Wavelet transform analysis of chromatin texture changes during heat shock

G. HERBOMEL*, A. GRICHINE*, A FERTIN‡, A. DELON†, C. VOURC'H*, C. SOUCHIER* & Y. USSON‡

**INSERM, IAB, University Grenoble Alpes, Grenoble, France*

†*CNRS, LIPHY, University Grenoble Alpes, Grenoble, France*

‡*CNRS, TIMC-IMAG, University Grenoble Alpes, Grenoble, France*

Key words. Chromatin, confocal fluorescence microscopy, heat shock, living cell, texture, wavelet.

Summary

Texture analysis can be a useful tool to investigate the organization of chromatin. Approaches based on multiscale analysis and in particular the 'à trou' wavelet analysis has already been used for microscopy (Olivo Marin). In order to analyse texture changes, the statistical properties of the wavelet coefficient images were summarized by the first four statistical orders: mean, standard deviation, skewness and kurtosis of the coefficient image histogram. The 'à trou' transform provided a representation of the wavelet coefficients and texture parameters with the same statistical robustness throughout the scale spaces. It was applied for quantifying chromatin texture and heat-induced chromatin changes in living cells. We investigated the changes by both laser scanning and spinning disk confocal microscopies and compared the texture parameters before and after increasing duration of heat shock exposure (15 min, 30 min and 1 h). Furthermore, as activation of the heat shock response also correlates with a rapid localization of HSF1 within a few nuclear structures termed nuclear stress bodies (nSBs), we compared the dynamics of nSBs formation with that of textural changes during 1 h of continuous heat shock. Next, we studied the recovery phase following a 1-h heat shock. Significant differences were observed, particularly affecting the perinucleolar region, even for the shortest heat shock time affecting mostly the skewness and standard deviation. Furthermore, progressive changes could be observed according to the duration of heat shock, mostly affecting fine details (pixel-wise changes) as revealed by the parameters, obtained from the first- and second-order wavelet coefficients. 'A trou' wavelet texture analysis provided a sensitive and efficient tool to investigate minute changes of chromatin.

Correspondence to: Yves Usson, Laboratoire TIMC-IMAG, Pavillon Le Taillefer, Domaine de la Merci, 38706 LA TRONCHE cedex. Tel: 33 4 56 52 00 74; fax: 33 4 56 52 00 22; e-mail: Yves.Usson@imag.fr or Claire Vourc'h, INSERM, IAB, University Grenoble Alpes, Grenoble, France. Tel: 33 4 76 54 94 70; fax: 33 4 76 54 94 14; e-mail: claire.vourch@ujf-grenoble.fr

Introduction

Nuclear texture analysis provides information about chromatin packing and nuclear organization. Chromatin consists mainly of DNA and histones. Several levels of chromatin organization have been described in the interphase nuclei starting from the fundamental nucleosomal unit made of 146 base pairs of DNA wrapped around a histone octamer, to higher order levels of organization (Felsenfeld & Groudine, 2003). Acetylation and deacetylation are important epigenetic post-translational modifications (PTM) targeting histones that locally affect histone dynamics, chromatin structure and their interaction with other partners (Julienne *et al.*, 2013; Ho *et al.*, 2014). Histone acetylation by HATs (histone acetyl transferase) is known to correlate with chromatin opening. Acetylated histones are enriched at euchromatic regions favouring binding of chromatin remodelling factors, transcription factors and gene expression (Bartova *et al.*, 2008). Conversely, deacetylation of histones by HDACs (histone deacetyl transferases) is associated with gene repression and correlates with condensed chromatin (heterochromatin). In living cells, global chromatin decondensation and increased chromatin accessibility occur in response to trichostatin A (TSA), a histone deacetylase (HDAC) inhibitor (Gorisch *et al.*, 2005; Rao *et al.*, 2007; Lleres *et al.*, 2009; Watson *et al.*, 2010). In addition, structural proteins, remodelling factors and histone variants are also known to modulate higher order chromatin structure (Misteli, 2010; Woodcock & Ghosh, 2010).

Chromatin remodelling is essential in the regulation of gene expression and is involved in fundamental cellular processes such as transcription in close coordination with DNA damage response (Bell *et al.*, 2011; Adam & Polo, 2014) and differentiation (Talwar *et al.*, 2013, Chen & Dent, 2014). Alteration of chromatin can result from mutations and miss-expression of associated proteins. In addition, chromatin structure is also sensitive to intracellular parameters such as calcium or ATP concentrations (Lleres *et al.*, 2009; Talwar *et al.*, 2013; Visvanathan *et al.*, 2013). It is therefore not surprising that

changes in higher order chromatin are often observed in malignant cells (Misteli, 2010; Fullgrabe *et al.*, 2011). In this general context, nuclear texture represents a relevant marker to assess diagnosis of human diseases (Weyn *et al.*, 1998; Van De Wouwer *et al.*, 2000; Murata *et al.*, 2002; Huisman *et al.*, 2005; Scheurer *et al.*, 2007).

In this work, we sought to analyse the consequences of environmental changes on chromatin texture. Heat-shock represents a relevant biological way to investigate chromatin remodelling events accompanying changes in gene expression. The heat shock response is triggered by temperature rise of a 5–7°C. It is accompanied by a global arrest of transcription and translation contrasting with the specific transcriptional activation of a small set of genes known as hsp 'heat shock protein' genes. Hsp gene activation is mediated by 'Heat Shock Transcription Factor 1' (HSF1), the key transcription factor of the heat shock response (Akerfelt *et al.*, 2010). In unstressed cells, HSF1 is present as a monomer. Upon heat shock, HSF1 trimerizes, undergoes posttranslational modifications and gains the capacity to bind DNA (Herbomel *et al.*, 2013). Interestingly, active HSF1 also accumulates within 1 μm nuclear structures in human cells, called nuclear Stress Bodies or nSBs (Biamonti & Vourc'h, 2010). nSBs represent sites of accumulation of HSF1 to pericentric regions enriched in repetitive satellite III (Sat III) sequences. Pericentric heterochromatin is transcriptionaly silent in unstressed cells. Upon stress, the HSF1 dependent activation of Sat III sequences results in the RNA polymerase II driven accumulation of long noncoding, stable RNAs. Sat III RNAs remain stably associated with the 9q12 loci (Jolly *et al.*, 2004; Eymery *et al.*, 2009; Eymery *et al.*, 2010). In contrast to the rest of the nucleus, chromatin at hsp genes and nSBs is acetylated in heat shocked cells (Thomson *et al.*, 2004; Fritah *et al.*, 2009).

Higher order chromatin structure has been studied using various biophysical approaches such as modelling of experiments to evaluate the impact of DNA sequence motifs (Arneodo *et al.*, 2011), linker lengths (Luque *et al.*, 2014), tail modifications and chromatin loops (Doyle *et al.*, 2014; Wang *et al.*, 2015). *In situ* approaches such as fluorescence *in situ* hybridization (FISH), chromosome conformation capture technology (3C, 4C, 5C, Hi-C) or FRET techniques have been carried out to measure proximity between DNA sequences (Dekker *et al.*, 2013; Belmont, 2014) or between nucleosomes (Lleres *et al.*, 2009). So far, methods based on chromatin texture analysis, though limited in resolution, have been mainly used to probe chromatin arrangement and detect changes in fixed or living cells (Huisman *et al.*, 2005; Depeursinge *et al.*, 2013). Most of these studies have been performed using Haralick co-occurrence matrices (Haralick *et al.*, 1973) and/or Galloway run-length matrices (Galloway, 1975). In these approaches, the grey-level dynamics has to be drastically reduced (in general down to 16 or even 8 grey levels) in order to limit the computation burden as well as the size of the co-occurrence matrices. This type of approach is indeed relevant when major

changes of texture, characterized by the presence of high contrasts, occur. However, when structural changes or changes of dynamics need to be explored over a very short period of time, the reduced grey level number may become a problem, causing small, though significant, changes of texture that are not detected.

Alternative approaches based on multiscale descriptors such as fractal descriptors (Bancaud *et al.*, 2012) and wavelet analysis (Bijaoui *et al.*, 1996; Van de Wouwer *et al.*, 1999; Van de Wouwer *et al.*, 2000; Olivo Marin, 2002) have also been introduced to analyse texture by microscopy approaches. So far, wavelet transformations have been more often used for image compression than for image analysis. However, development of open source image analysis softwares such as ImageJ (Rasband WS, National Institutes of Health, Bethesda, Maryland, USA, http://imagej.nih.gov/ij/) makes it now possible to use this type of powerful process for the quantification of microscopy images (Unser, 2014). Briefly, wavelet transformations have been used to decompose images of the nuclear texture into images (coefficient images) of various scales, from fine details to large identified structures. Usually, only the respective energies of the wavelet coefficients (i.e. the integrals of the coefficient images) have been used for texture analysis. In our study, we have extended the number of texture descriptors by taking advantage of the first four orders of the statistical distribution of the coefficient images: mean, standard deviation, skewness and kurtosis. Furthermore, we have used a variant of the wavelet transform called 'à trou' transform (Bijaoui *et al.*, 1996; Olivo Marin, 2002). Our objective was twofold: on the first hand, we wanted a representation of the wavelet coefficients making it possible to obtain a direct visual interpretation, on the second hand we sought to provide texture parameters with the same statistical robustness throughout the scale spaces (images of wavelet coefficients). In contrast to the classical wavelet, in the 'à trou' algorithm, the size of the image grid is not modified whereas the kernel of the convolution wavelet is dilated between the decomposition steps. This provides the advantage of keeping a constant number of pixels involved in the calculation of the histogram of wavelet coefficient whatever the step of decomposition. Therefore, the higher order moments have the same statistical robustness for all steps and can be directly compared.

In this paper the 'à trou' wavelet transform was applied to the study of heat-induced chromatin changes. We investigated the gross nuclear texture changes induced by heat shock, the effect of heat shock duration, and the dynamics of texture changes during induction and recovery.

Materials and methods

Cell culture

Human HeLa cells were transfected using Lipofectamine 2000 (Invitrogen, Carlsbad, CA, USA) and constructs expressing

the core histone H2A fused to the eGFP auto-fluorescent protein. Stable eGFP-H2A cell line was selected and was grown in DMEN supplemented with 10% fetal bovine serum, 0.1 mg mL^{-1} streptomycin and 1 mM L-glutamine (Invitrogen). For measurement, cells were plated on Lab-Tek I chambered cover-glass (Nunc, Roskiklde, Denmark) or Delta T dish (Bioptechs, Butler, PA, USA) and were observed in cell medium without phenol red.

CLSM image acquisition

Nuclear texture images were first acquired on a confocal laser scanning microscope (Confocor II, Zeiss, Iena, Germany) equipped with a X40 C-Apochromat water immersion objective (NA = 1.2). The eGFP-H2A protein was excited with a 488 nm argon ion line and the fluorescence emission was recorded through a 505-nm long pass filter (LP). The pinhole size was adjusted to 1 Airy unit. To decrease noise, four images of each section were averaged. Thirty optical sections were collected through an entire cell nucleus of living cells with a 0.5 μm between sections. The pixel size was equal to 112 nm x 112 nm. During the experiments, cells were maintained at 37°C in an atmosphere containing 5% CO_2, using a small incubator system (Zeiss). Heat shock was performed at 42°C on a heating plate close to the microscope. The heating time was equal to 15 min, 30 min or 1 h. Under stress, the response is very fast and occurs within a few minutes (Eymery *et al.*, 2010). One hour heat shock is commonly used stress duration and using this condition the response is reversible (Jolly *et al.*, 1997). In order to check heat shock efficiency, the formation of nSBs was detected *in situ* through immunofluorescence or HSF1-tagRFP-T expression. Cells analysed before heat shock were relocated and analysed after heat shock. For the texture analysis, five neighbour optical slices were selected in the middle of the nucleus.

Spinning disk image acquisition

Complementary studies were performed using a spinning disk confocal laser microscopy system (Andromeda iMIC, FEI, Munich, Germany), equipped with a X63 plan-apochromat oil immersion objective (NA = 1.46) and an EMCCD camera (iXon3 897, Andor, Belfast, UK). Heat shock was performed directly on the microscope stage using the Delta T open dish system (Bioptechs) which uses electrical resistance heating via thin film bottom coating of the cell dish. Long heat shock recovery was followed using a heating and incubation system (Ibidi GmbH, Martinsried, Germany). A 488-nm diode laser was used to excite the fluorescence of eGFP-H2A proteins then a 561-nm solid state laser was used to excite the fluorescence of HSF1-mRFP-T proteins. The fluorescence emission signals were recorded sequentially, through a 405/488/561 dichroic slider and a 446/523/600/677 emission filter. The pixel size was equal to 100×100 nm and the axial step was 300 nm.

For each time point a stack of 30 planes was recorded with the exposure time 100 ms per frame and electronic gain 100×, no sign of photobleaching was observed in either fluorescence channel. Acquisition was limited to three microscopy fields in order to cumulate data obtained at a very similar time (<50 s). For the texture analysis, eleven neighbour optical slices were selected in the middle of the stack.

Wavelet transformation

The wavelet transform decomposes a signal in a series of coefficients on an orthogonal basis, which describe the local contrasts at various scales and a final so-called wavelet plane, which describes the final residuals. The type of contrast that is measured is characterized by the properties of the selected wavelet. In the case of fluorescence texture analysis of nuclei, we used a Gaussian kernel as the basis for the decomposition wavelet. We used the '*à trou*' wavelet decomposition (Bijaoui *et al.*, 1996; Olivo Marin, 2002) which is better suited for the calculation of our texture parameters (see Appendix).

Prior to wavelet decomposition, the intensities of the pixels were standardized with respect to the mean intensity and standard deviation in the whole nucleus. This was done in order to obtain texture information that is not depending on a global difference of intensity in the fluorescence signal between 3D series or instabilities in the acquisition process. However, before performing this standardization we calculated the global coefficient of variation of grey levels to provide a global measurement of the chromatin organization.

Figure 1 shows an example of the '*à trou*' decomposition of a 2D section of a nucleus where each image (Figs. 1C and D) is that of the wavelet coefficients calculated at a given scale (from fine to gross resolution). The texture parameters that we measured are the first four statistical moments of the distribution (Fig. 1E) of the wavelet coefficients (i.e. contrast levels) at each scale. In practice, we considered the first five coefficient images (named C1–C5 and corresponding to space scales 0.22, 0.45, 0.90, 1.79 and 3.58 μm), which gives a total of 20 texture parameters: mean, standard deviation, skewness and kurtosis for C1–C5.

However, an important issue had to be solved for the calculation of the wavelet transform. The objects of interest (i.e. the nuclei) are spatially bounded and do not extend over the full size of the image whereas the wavelet transform is global. As a consequence the wavelet coefficients calculated on the pixels located close the nuclear membrane are influenced by outside information (black background), furthermore for high order wavelets (C4 and C5) the wavelet coefficients within a given nucleus can even be influenced by the information from another nucleus located in its immediate neighbourhood. In order to avoid the interference of information coming from different nuclei within the same image, the first processing consisted in extracting each nucleus from the image and in transferring them into separate vignette images. This way,
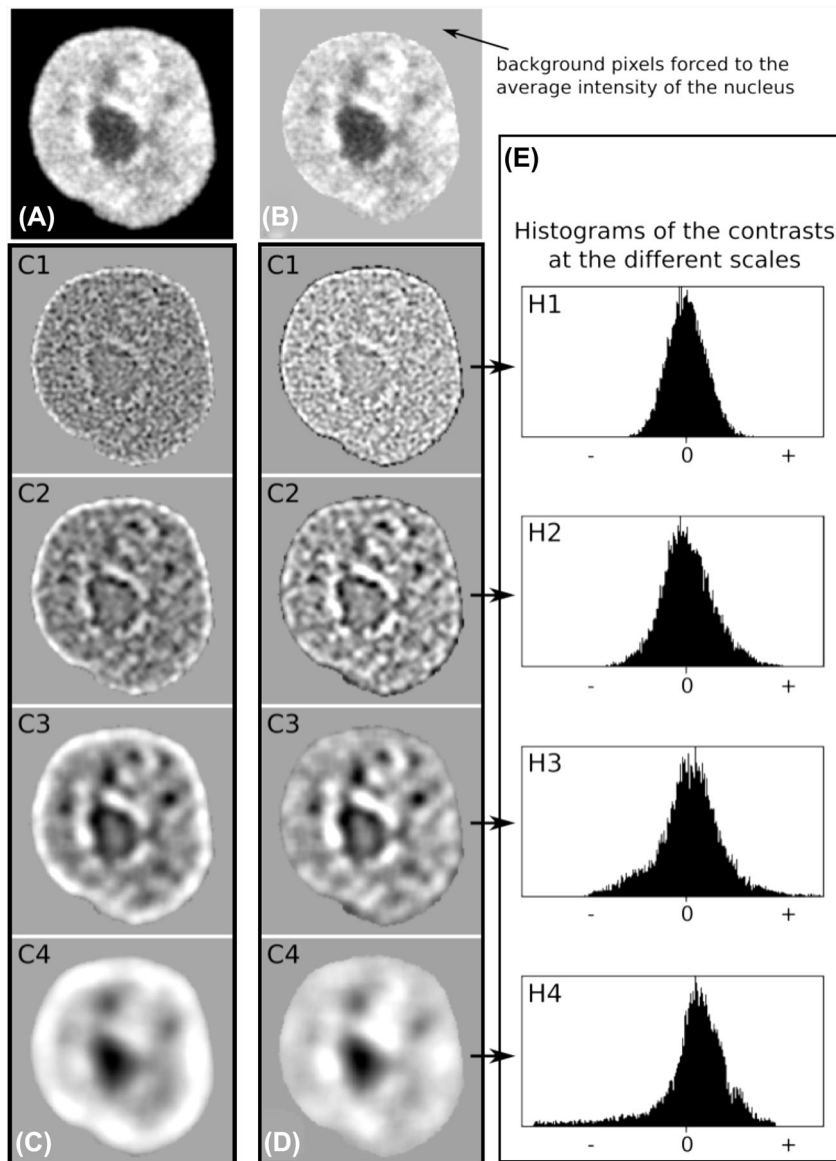
Fig. 1. Example of wavelet decomposition. (A) 2D fluorescence image of a section through a nucleus. (B) Modified image, pixels of the background are set to the average intensity of the nucleus. (C) Images of the first four wavelet coefficients obtained for image A. (D) Images of the first four wavelet coefficients obtained for image B. Right column: histograms (H1–H4) of the wavelet coefficient values within the nucleus for the corresponding wavelet images (C1–C4). The measured texture parameters are the first four moments of the histograms: mean, standard deviation, skewness and kurtosis.

the vignette images could be processed and analysed without interference.

Next, it was necessary to preprocess the vignette images in order to alleviate the influence of the background. Figure 1(C) shows the first four wavelet coefficient images obtained from the 'à trou' transform of a single image vignette (Fig. 1A) without preprocessing. It can be seen that the pixels of the nucleus located close to the edge were brighter than the other pixels. This is because the background pixels surrounding the nucleus were taken into account during the wavelet calculation. Therefore, the edge of the nucleus was detected as a strong discontinuity in the image and this created a so-called 'ripple' or 'ringing' effect inside the nucleus. This ringing does not describe the actual chromatin texture and contaminates the useful texture information. In order to alleviate this effect, we processed the vignette images (Fig. 1A) as follows: (i) the image was segmented in order to extract the binary mask of the nucleus, (ii) the average grey level of the nucleus was measured through this binary mask and (iii) the background pixels (i.e. those outside the binary mask) were set to a grey-level equal to the average grey level of the nucleus. This way, the background pixels have a negligible influence on the

wavelet coefficients calculated for the nuclear pixels close to the edge. Figure 1(D) shows the result of wavelet decomposition performed on the preprocessed vignette image (Fig. 1B). The edge ringing disappeared and now the wavelet coefficients calculated within the pixels close to the edge of the nucleus are relevant to the nucleus texture.

For the texture analysis in the nucleus volume, we performed wavelet analyses on neighbour optical slices selected in the middle of the stack. The final histograms of wavelet coefficients used for parameter calculations were obtained by pooling the histograms obtained for each of section planes.

The same nuclei were acquired in 3D and analysed before and after heat shock. Statistical analysis was performed using Stata/IC statistics/data analysis software (StataCorp, TX, USA).

Nuclear stress bodies

Nuclear stress bodies were automatically detected using ImageJ software. The segmentation threshold was defined using the MaxEntropy method and despeckled using 3×3 median filter. The process was applied on each section plane. Measurement of the total projected area of nSBs was performed on the cumulative projection of the whole stack of images (Z projected image).

Results

Parameters to analyse heat-induced textural changes

Nuclei were imaged before and after a 1-h heat shock. Their textures were expressed with four parameters for each of the five coefficient planes (C1–C5). These parameters were the first four statistical moments of the coefficient histograms: mean, standard deviation, skewness and kurtosis. Textural changes between pre- and postheat shock were investigated by a multivariate analysis. Nuclear texture images were split by the '*à trou*' wavelet transform into five coefficient images corresponding to contrasts at various scales, from fine to gross details (Fig. 1) and were measured. As summarized in Table 1, nearly all parameters were highly significant. The mean value and the skewness were higher following heat shock whatever the wavelet scale. Meanwhile, the standard deviation was higher following heat shock only at high scales (C4 and C5). As assessed by paired *t*-test values, kurtosis over all scales and parameters for scale C5 were the least significant parameters.

Impact of heat-shock duration on the evolution of textural changes

Changes of nuclear texture were then analysed in cells submitted to 15 min, 30 min or 1 h heat shock. Figure 2 shows some examples of the same nuclei before (left column) and after heat shock (right column). The data are presented in Ta-

ble 1. Interestingly, in all nuclei, nuclear texture appeared as more heterogeneous after heat shock, whereas in contrast, an accentuation of dense chromatin areas around the nucleoli and at the vicinity of the nuclear membrane was observed. In all cases a statistically significant change of texture parameters altogether was observed (paired Hotelling's *T*-squared test, $p < 0.001$).

Data analyses showed that stress-induced variations of the three first parameters were observed at small spatial scales: skew C1, skew C2 and kurt C1 for HeLa cell line; skew C3, skew C2 and mean C1 in U20S cell line (data not shown).

Heat-induced chromatin changes were then also analysed in a U2OS human cell line. Despite significant differences in their nuclear textural parameters, both HeLa and U2OS cell lines responded to a 1-h heat shock in a similar way. Data analyses showed that the three first parameters that changed upon heat shock were observed at small (C1 and C2) spatial scales: skew C1, skew C2 and kurt C1 for HeLa cell line; skew C3, skew C2 and mean C1 in U20S cell line.

The three groups of cells corresponding to the different time of stress exposure were clearly identified with discriminant analysis and a progressive impact of the heat-shock duration was observed (Fig. 3). The first discriminant factor was highly significant. The parameters correlated with the first discriminant factor were similar to those exhibiting the highest *F* values of the ANOVA test (Table 1, last column). Therefore, among all our texture parameters, some (mean C1, stdv C1, skew C1, kurt C1, mean C2 and skew C2) were better to translate the evolution of textural patterns due to stress duration. It appeared that the first wavelet coefficients (C1 and C2) accounted for most of the changes related to the stress duration. Because C1 and C2 corresponded to the highest spatial frequencies this means that the changes involved fine details of the chromatin.

Correlation between textural changes and nSB formation

The kinetics of evolution of textural changes upon heat shock was correlated to the kinetics of formation of nSBs. To this end, we used a spinning disk system equipped with a system making it possible to perform sequential acquisitions without bleaching on cells submitted to a continuous heat shock. Acquisitions were performed at 5-min intervals during 1 h at 37°C followed by 1 h at 42°C. The successive acquisitions in unstressed and stressed cells were used to estimate the impact of two successive acquisitions on the texture itself. All the differences between two successive acquisitions ($\delta = 5$ min) were calculated. As expected, the differences ($n = 156$) we observed, except for three of them (mean C4, mean C5 and stdv C5) were highly significant in the heat-shock phase. Significant differences ($n = 144$) were also observed in the nonheat-shock phase for the following parameters: CV, skew C1, skew C2, stdv C2, stdv C3 and kurt C5. However, in these cases, differences were of lower amplitude (2- to 5-folds) than the differences observed in the heat-shock phase.

Table 1. Differences in size and in texture parameters between nonheat-shocked and heat-shocked cells (mean ± SEM)

Variables	NHS: 15-min HS	NHS: 30-min HS	NHS: 1-h HS	ANOVA *F*-value
Cell number	46	45	49	
Cross–section area (μm^2)	15.09 ± 1.61	17.45 ± 2.25	19.38 ± 1.93	1*
Fl. Coefficient variation	−0.061 ± 0.008	−0.071 ± 0.004	−0.148 ± 0.004	72
Mean C1	−0.002 ± 0.000	−0.003 ± 0.000	−0.006 ± 0.000	89
Standard deviation C1	0.022 ± 0.001	0.029 ± 0.002	0.039 ± 0.001	41
Skewness C1	−0.066 ± 0.049*	−0.222 ± 0.023	−0.815 ± 0.033	119
Kurtosis C1	0.547 ± 0.267	0.969 ± 0.111	3.060 ± 0.243	38
Mean C2	−0.002 ± 0.000	−0.004 ± 0.000	−0.007 ± 0.000	120
Standard deviation C2	0.017 ± 0.001	0.020 ± 0.002	0.017 ± 0.001	1*
Skewness C2	−0.130 ± 0.029	−0.232 ± 0.020	−0.604 ± 0.021	114
Kurtosis C2	0.054 ± 0.055*	−0.122 ± 0.056	−0.425 ± 0.100	11
Mean C3	−0.003 ± 0.000	−0.006 ± 0.001	−0.011 ± 0.001	73
Standard deviation C3	−0.001 ± 0.002*	−0.002 ± 0.001*	−0.015 ± 0.002	24
Skewness C3	−0.214 ± 0.022	−0.293 ± 0.027	−0.451 ± 0.024	24
Kurtosis C3	−0.302 ± 0.077	−0.554 ± 0.109	−0.942 ± 0.103	11
Mean C4	−0.006 ± 0.001	−0.010 ± 0.001	−0.012 ± 0.001	22
Standard deviation C4	−0.010 ± 0.002	−0.017 ± 0.002	−0.020 ± 0.002	8
Skewness C4	−0.195 ± 0.029	−0.144 ± 0.030	−0.273 ± 0.030	5
Kurtosis C4	0.036 ± 0.077*	−0.173 ± 0.080	−0.284 ± 0.092	4
Mean C5	−0.006 ± 0.001	−0.007 ± 0.001	−0.005 ± 0.001	3
Standard deviation C5	−0.009 ± 0.002	−0.012 ± 0.002	−0.006 ± 0.002	2*
Skewness C5	−0.009 ± 0.039*	0.073 ± 0.035	−0.043 ± 0.044*	2*
Kurtosis C5	0.310 ± 0.106	0.146 ± 0.070	0.076	2*

*Nonsignificant value ($p = 0.05$).

On average, the relocation of HSF in nuclear stress bodies became visible from 6.25 min and the Z projected areas of all the nSBs in the nuclei increased according to the duration of the heat shock (Fig. 4). Textural changes were also observed at shortest time (5-min heat shock) and increased according to the duration of the heat shock (Figs. 5A and C). The main changes were observed for the skewness (that can be interpreted as the balance between bright and dark contrasts) parameters, the values of which increased over time, although with a smaller amplitude for the first and fifth wavelet coefficients C1 and C5 (Fig. 5A). Furthermore, significant changes were also observed for the standard deviation (that can be interpreted as the global contrast) however these changes were less correlated through the scales. As a matter of fact, a decrease was observed for wavelet coefficient C1, whereas an increase was observed for both C3 and C4 (Fig. 5C). The combined changes of the skewness and standard deviation mainly occurring at intermediate scales would translate an increased localization of the fluorescence around the nucleoli. Next we studied the recovery phase following a 1-h heat shock at 42°C (Figs. 5B and D). A similar optical set up was used but under 5% CO2 environment. We observed that the skewness parameters were still increasing during the first hour of recovery, and then exhibited a significant decay (Fig. 5B) at a time the standard deviations had already returned to their initial values (shorter that 1 h after the end of heat shock) (Fig. 5D). On average,

the onset of the skewness decay phase was concomitant with the disappearance of nuclear stress bodies and was observed in these cells after 1.25 h of recovery.

Discussion

Several different factors are likely to account for variations in nuclear texture. In this work, the same cells were imaged over the course of the heat-shock response and the evolution of the nuclear texture analyzed through paired *t* tests. This approach is more prone to reveal subtle variations, than when different sets of cells are compared. Besides heat shock, other factors, such as acquisition process, cell cycle progression, can infer in the evolution of textural parameters. However, our data clearly show that heat shock is the main factor contributing to the differences of texture we observe.

In this work, a '*à trou*' wavelet method was applied to texture analysis. Such a multiresolution approach presents the advantage of identifying the main scale of chromatin transformation. The four first moments extracted from the histogram of the wavelet coefficients complete the information: the kurtosis is a measure of flatness or peakness, compared to a Gaussian histogram, the skewness is a measure of symmetry (and therefore a measure of chromatin condensation when positive) and the standard deviation a measure of variability (higher, when positive and negative contrasts are both present). Skewness values
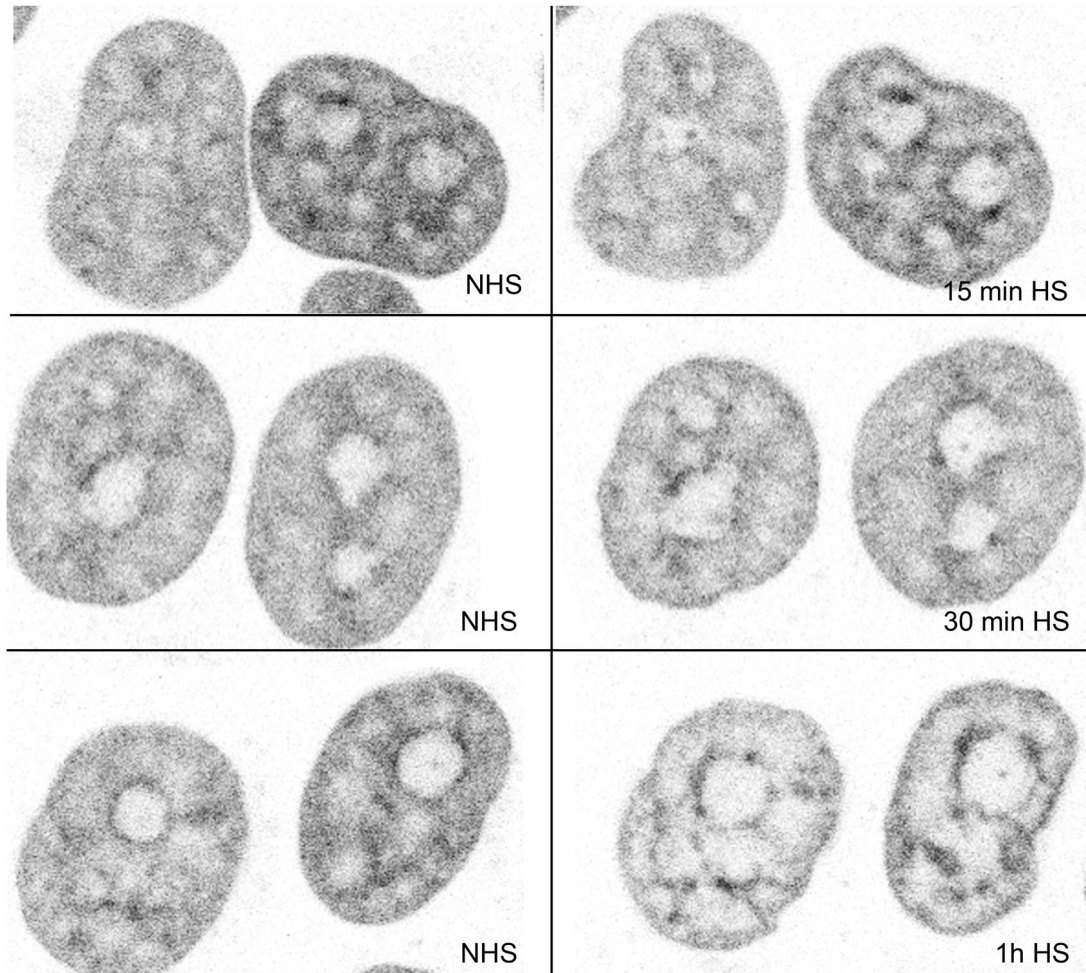
Fig. 2. Heat-shock-induced changes of chromatin texture. The same cells were observed before (NHS) and after 15 min, 30 min or 1-h heat shock (HS). The contrast of fluorescence images was inverted.

we observe are therefore likely to reveal increased chromatin compaction. Similarly, increased standard deviation value, at low and intermediate scales, reveals increased heterogeneity of chromatin texture caused by heat shock. The evolution of both parameters is in good agreement with the contrasting impact of heat shock on gene expression. The global repression of gene expression on one hand is counter-balanced by the burst of transcription of pericentric heterochromatin, primarily on chromosome 9, leading to a contrasted histone acetylation distribution: foci of acetylated chromatin develop over a global deacetylated nucleus (Jolly *et al.*, 2004; Fritah *et al.*, 2009). Based on our wavelet analysis, higher order chromatin organization appears as a concomitant event to nSBs formation since a significant chromatin remodelling is already detected at the early phase of the heat-shock response. Although cause and consequence are often difficult to discern, it is however tempting to speculate that the HSF1-dependent recruitment of histone acetyl transferases and of RNA pol II at nSBs contributes to global chromatin hypoacetylation and

downregulation of gene expression observed in the rest of the nucleus (Biamonti & Vourc'h, 2010).

Interestingly, our work identifies major modifications of chromatin texture at the perinucleolar region, with increased chromatin density at these regions. Nucleoli correspond to sites of rRNA synthesis. In addition, the presence of non-rDNA gene arrays, within or close to the nucleoli, has also been identified through genomic analysis, demonstrating that 4% of the entire genome sequences interacts with nucleoli of HeLa cells. These sequences correspond to pericentric and centromeric repetitive sequences, to regions with low gene density and to regions significantly enriched in transcriptionally repressed genes (Guetg & Santoro, 2012; Padeken & Heun, 2014).

The reason why a higher chromatin density appears at the nucleolar periphery in heat-shocked cells is still unclear at present. The nucleolus has already been identified as an important marker of stress and most stressing situations, including heat shock, are accompanied by a reorganization of this nuclear compartment (Boulon *et al.*, 2010; Jacob *et al.*, 2013).
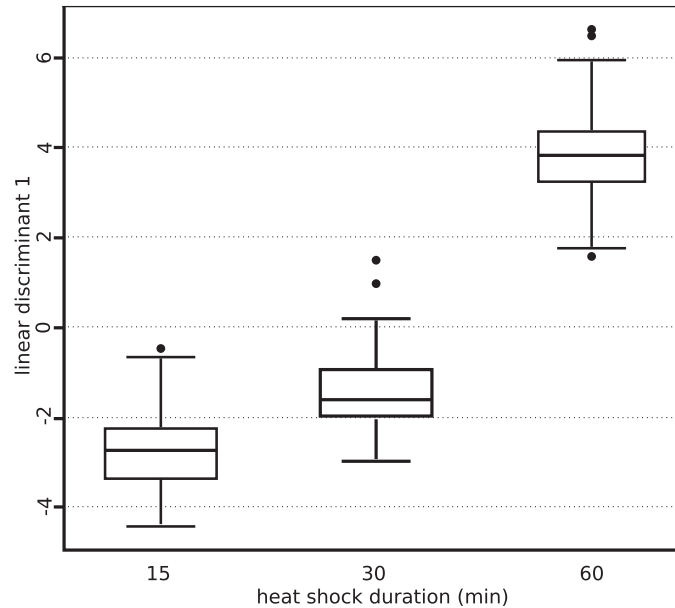
Fig. 3. Analysis of texture changes as function of heat-shock duration. Box-plots of the first score resulting from a discriminant analysis. A significant discrimination of the heat-shock groups can be observed in accordance with the heat-shock duration.
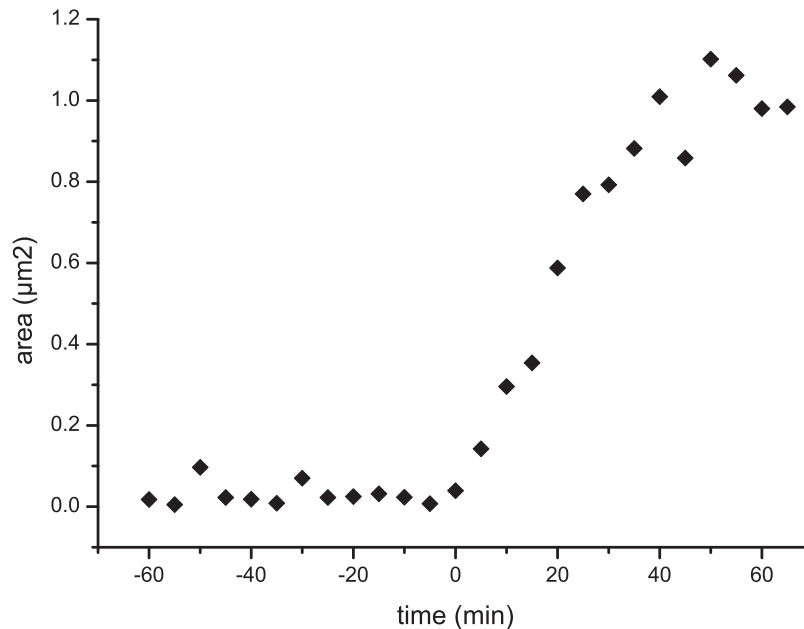

Fig. 4. Formation of the nuclear stress bodies during 1-h heat shock. Nuclear stress bodies labelled by HSF1-tagRFP-T were automatically detected and the mean Z projected areas of all the nSBS were measured every 5 min in HeLa cells ($n = 12$). Acquisitions were performed during 2 h. The cells had no stress in the first hour ($t = -60$ to 0 min), and they were exposed to heat shock in the second one ($t = 5$ to 60 min).

The nucleolus contains three different structures: the fibrillar centre (FC) corresponding to the sites where tandem repeats of the rDNA transcription units are located and where transcription of rDNA occurs, the dense fibrillar centre (DFC) where RNA are stored and the granular centre (GC) where assembly of rRNA with ribosomal proteins takes place. Several stressing conditions lead to a reorganisation of the nucleolus characterized by the condensation and subsequent segregation, of the FC and GC, that remain juxtaposed, together with the formation of nucleolar caps around the nucleolar remnants (Shav-Tal *et al.*, 2005; Boulon *et al.*, 2010). Interestingly, the nature of the nucleolar remodelling events depends on the nature of the stress perceived by the cell (Shav-Tal *et al.*, 2005; Boulon *et al.*, 2010; Jacob *et al.*, 2013).
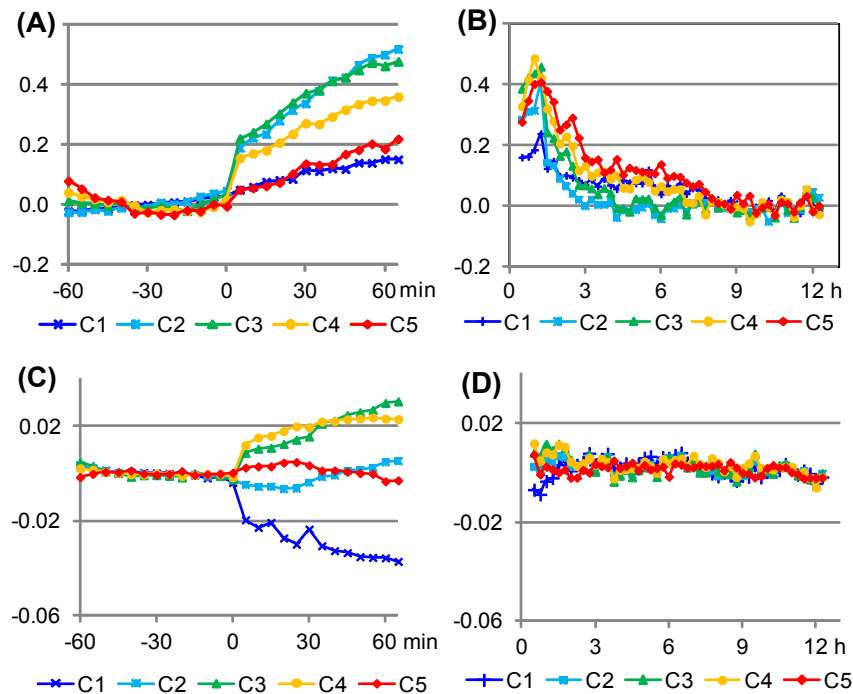
Fig. 5. Evolution of the nuclear texture in the course of the heat-shock response. Mean changes of H2A-eGFP texture in HeLa cells ($n = 12$ cells). (A) Skewness parameter for coefficient C1–C5, prior and during heat shock. Acquisitions were performed at 5-min intervals during 1 h at 37°C (nonheat-shocked cells) followed by 1 h of continuous heat shock at 42°C ($t \geq 5$) under the microscope. The start of the heat shock corresponds to time = 0. (B) Skewness parameter during recovery phase starting 30 min (time = 0) after the end of a 1-h heat shock. Acquisitions were performed at 15-min intervals during 12 h. (C) Standard deviation parameter for coefficient C1–C5: same nuclei and same acquisitions as in A. (D) Standard deviation parameter during recovery phase: same nuclei and same acquisitions as in B.

Perinucleolar rings we observed also resemble those detected in bovine senescent cells using propidium iodide, or immunofluorescence analysis against H3K9me3 (Pichugin *et al.*, 2011). In mouse, perinucleolar rings are also present in early embryos, before the formation of nuclear clusters of pericentric heterochromatin also known as chromocenters (Probst *et al.*, 2010). Interestingly, besides heat shock, early development (Probst *et al.*, 2010) and senescence (Enukashvily *et al.*, 2007) represent contexts where pericentric heterochromatin is transcriptionaly competent. The functional signification of this redistribution involving heterochromatin itself, rRNA genes or other noncoding regions should definitely be further explored in the future.

Conclusion and perspectives

In conclusion, the '*à trou*' wavelet analysis represents a simple and efficient tool to investigate changes of chromatin structure at any scales and may be usefully applied to various textured biological structures either at the cell or tissue scales. Using the heat-shock response as a model, we show that this approach allows the detection of significant changes in chromatin texture, even at the early onset of the heat-shock response where changes in chromatin texture cannot be detected through

visual inspection. As expected, we show that the extent of chromatin remodelling increases with the duration of heat exposure. Whether the transient recruitment and sequestration of important actors such as histone acetyl transferases to nSBs (Jolly *et al.*, 2004) plays an active role in global chromatin remodelling events remains to be established. Interestingly, our data indicate that the kinetics of disappearance of nSBs following heat-shock correlates with the inversion of the skewness parameter. The tools we have developed should now allow us to perform a more precise analysis of the kinetics of nSBs formation and of chromatin remodelling using different time exposure and/or intensity of stress. This possibility should help us to define the role of nSBs in global chromatin remodelling in the heat-shock response.

Acknowledgements

(CIBLE 2009) and by the French cancer research association (ARC) under contracts 3686 and EML20120905281.

Appendix

Discrete implementation of 2D wavelet decomposition

$$c_{i+1}(x, y) = \Sigma_n \Sigma_m h(n, m) c_i(2x + n - d/2, 2y + m - d/2),$$

where c is a wavelet coefficient image, x and y the discrete coordinates of a pixel, i the rank of the wavelet coefficient, h is a d by d wavelet kernel and n and m are ranging from 0 to $d-1$, with d an odd integer.

As a consequence in this usual discrete wavelet decomposition there is dyadic scale reduction from c_i to c_{i+1}, that is, the number of rows and columns is divided by two and the total number of pixels is divided by four from one coefficient image to the next one.

'A trou' decomposition

$$c_{i+1}(x, y) = \Sigma_n \Sigma_m h(n, m) c_i(x + (n - d/2) 2^i, y + (m - d/2) 2^i).$$

In contrast to the classic decomposition, the '*à trou*' decomposition preserves the total number of pixels. Therefore, there is no scale change from c_i to c_{i+1}. This offers many advantages listed by Bijaoui *et al.* (1996). In our case, the statistical moments of the histograms of the coefficient images are built with the same number of pixels and offer the same statistical robustness.

For our study we use a 3×3 Gaussian-like kernel g:

$$g = [[1/16, 1/8, 1/16] [1/8, 1/4, 1/8] [1/16, 1/8, 1/16]].$$

However, using directly this kernel as a wavelet kernel would not satisfy the condition of orthogonal basis of the co-efficient planes. In order to satisfy this condition the wavelet decomposition using g is finally written with the following equations:

$$p_{i+1}(x, y) = \Sigma_n \Sigma_m g(n, m) p_i(x + (n - d/2) 2^i, y + (m - d/2) 2^i)$$
$$c_{i+1}(x, y) = p_i(x, y) - p_{i+1}(x, y)$$

with p_i the wavelet plane image and p_0 the initial image.

Considering that convolving a wavelet plane image p_i by the kernel g operates a smoothing, that is, a equivalent to a lowpass filtering, then subtracting the result of this smoothing from p_i is equivalent to submitting it to bandpass filtering. Therefore,

the complete '*à trou*' wavelet decomposition using kernel g can be compared to a decomposition of the image by a bank of octave bandpass filters.

References

Adam, S. & Polo, S.E. (2014) Blurring the line between the DNA damage response and transcription: the importance of chromatin dynamics. *Exp. Cell Res.* **329**, 148–153.

Akerfelt, M., Morimoto, R.I. & Sistonen, L. (2010) Heat shock factors: integrators of cell stress, development and lifespan. *Nat. Rev. Mol. Cell Biol.* **11**, 545–555.

Arneodo, A., Vaillant, C., Audit, B., Argou, F., d'Aubenton-Carafa, Y. & Thermes, C. (2011) Multi-scale coding of genomic information: From DNA sequence to genome structure and function. *Phys. Rep.* **498**, 45–188.

Bancaud, A., Lavelle, C., Huet, S. & Ellenberg, J. (2012) A fractal model for nuclear organization: current evidence and biological implications. *Nucl. Acids Res.* **40**, 8783–8792.

Bartova, E., Krejci, J., Harnicarova, A., Galiova, G. & Kozubek, S. (2008) Histone modifications and nuclear architecture: a review. *J. Histochem. Cytochem.* **56**, 711–721.

Bell, O., Tiwari, V.K., Thoma, N.H. & Schubeler, D. (2011) Determinants and dynamics of genome accessibility. *Nat. Rev. Genet.* **12**, 554–564.

Belmont, A.S. (2014) Large-scale chromatin organization: the good, the surprising, and the still perplexing. *Curr. Opin. Cell Biol.* **26**, 69–78.

Boulon, S., Westman, B.J., Hutten, S., Boisvert, F.M. & Lamond, A.I. (2010). The nucleolus under stress. *Mol. Cell* **40**, 216–227.

Biamonti, G. & Vourc'h, C. (2010) Nuclear stress bodies. *Cold Spring Harb. Perspect. Biol.* **2**, a000695.

Bijaoui, A., Slezak, E., Rue, F. & Lega, E. (1996) Wavelets and the study of the distant universe. *Proc. IEEE Spec. Issue Wavelets* **84**, 670–679.

Chen, T. & Dent, S.Y. (2014) Chromatin modifiers and remodellers: regulators of cellular differentiation. *Nat. Rev. Genet.* **15**, 93–106.

Dekker, J., Marti-Renom, M.A. & Mirny, L.A. (2013) Exploring the three-dimensional organization of genomes: interpreting chromatin interaction data. *Nat. Rev. Genet.* **14**, 390–403.

Depeursinge, A., Foncubierta-Rodriguez, A., Van De Ville, D. & Muller, H. (2013) Three-dimensional solid texture analysis in biomedical imaging: review and opportunities. *Med. Image Anal.* **18**, 176–196.

Doyle, B., Fudenberg, G., Imakaev, M. & Mirny, L.A. (2014) Chromatin loops as allosteric modulators of enhancer-promoter interactions. *PLoS Comput. Biol.* **10**, e1003867.

Enukashvily, N.I., Donev, R., Waisertreiger, I.S. & Podgornaya, O.I. (2007) Human chromosome 1 satellite 3 DNA is decondensed, demethylated and transcribed in senescent cells and in A431 epithelial carcinoma cells. *Cytogenet. Genome Res.* **118**, 42–54.

Eymery, A., Horard, B., El Atifi-Borel, M. *et al.* (2009) A transcriptomic analysis of human centromeric and pericentric sequences in normal and tumor cells. *Nucl. Acids Res.* **37**, 6340–6354.

Eymery, A., Souchier, C., Vourc'h, C. & Jolly, C. (2010) Heat shock factor 1 binds to and transcribes satellite II and III sequences at several pericentromeric regions in heat-shocked cells. *Exp. Cell. Res.* **316**, 1845–1855.

Felsenfeld, G. & Groudine, M. (2003) Controlling the double helix. *Nature* **421**, 448–453.

Fritah, S., Col, E., Boyault, C. *et al.* (2009) Heat-shock factor 1 controls genome-wide acetylation in heat-shocked cells. *Mol. Biol. Cell* **20**, 4976–4984.

Fullgrabe, J., Kavanagh, E. & Joseph, B. (2011) Histone onco-modifications. *Oncogene* **30**, 3391–3403.

Galloway, M.M. (1975) Texture analysis using gray level run lengths. *Comp. Graph. Image Process* **4**, 172–179.

Gorisch, S.M., Wachsmuth, M., Toth, K. ., Lichter, P. & Rippe, K. (2005) Histone acetylation increases chromatin accessibility. *J. Cell Sci.* **118**, 5825–5834.

Guetg, C. & Santoro, R. (2012) Formation of nuclear heterochromatin: the nucleolar point of view. *Epigenetics* **7**, 811–814.

Haralick, R.M., Shanmugam, R. & Dinstein, I. (1973) Textural Features for Image Classification. *IEEE Trans Syst., Man Cyber.* **3**, 610–621.

Herbomel, G., Kloster-Landsberg, M., Folco, E.G., Col, E., Usson, Y., Vourc'h, C., Delon, A. & Souchier, C. (2013) Dynamics of the full length and mutated heat shock factor 1 in human cells. *PLoS One* **8**, e67566.

Ho, J.W., Jung, Y.L., Liu, T. *et al.* (2014) Comparative analysis of metazoan chromatin organization. *Nature* **512**, 449–452.

Huisman, A., Ploeger, L.S., Dullens, H.F., Poulin, N., Grizzle, W.E. & van Diest, P.J. (2005) Development of 3D chromatin texture analysis using confocal laser scanning microscopy. *Cell. Oncol.* **27**, 335–345.

Jacob, M.D., Audas, T.E., Uniacke, J., Trinkle-Mulcahy, L. & Lee, S. (2013) Environmental cues induce a long noncoding RNA-dependent remodeling of the nucleolus. *Mol. Biol. Cell* **24**, 2943–2953.

Jolly, C., Metz, A., Govin, J., Vigneron, M., Turner, B.M., Khochbin, S. & Vourc'h, C. (2004) Stress-induced transcription of satellite III repeats. *J. Cell Biol.* **164**, 25–33.

Jolly, C., Morimoto, R., Robert-Nicoud, M. & Vourc'h, C. (1997) HSF1 transcription factor concentrates in nuclear foci during heat shock: relationship with transcription sites. *J. Cell Sci.* **110**(Pt 23), 2935–2941.

Julienne, H., Zoufir, A., Audit, B. & Arneodo, A. (2013) Human genome replication proceeds through four chromatin states. *PLoS Comput. Biol.* **9**, e1003233.

Lleres, D., James, J., Swift, S., Norman, D.G. & Lamond, A.I. (2009) Quantitative analysis of chromatin compaction in living cells using FLIM-FRET. *J. Cell Biol.* **187**, 481–496.

Luque, A., Collepardo-Guevara, R., Grigoryev, S. & Schlick, T. (2014) Dynamic condensation of linker histone C-terminal domain regulates chromatin structure. *Nucl. Acids Res.* **42**, 7553–7560.

Misteli, T. (2010) Higher-order genome organization in human disease. *Cold Spring Harb. Perspect. Biol.* **2**, a000794.

Murata, S., Mochizuki, K., Nakazawa, T. *et al.* (2002) Detection of underlying characteristics of nuclear chromatin patterns of thyroid tumor cells using texture and factor analyses. *Cytometry* **49**, 91–95.

Olivo Marin, J.C. (2002) Extraction of spots in biological images using multiscale products. *Patt. Recogn.* **35**, 1989–1996.

Padeken, J. & Heun, P. (2014). Nucleolus and nuclear periphery: velcro for heterochromatin. *Curr. Opin. Cell Biol.* **28**, 54–60.

Pichugin, A., Beaujean, N., Vignon, X. & Vassetzky, Y. (2011) Ring-like distribution of constitutive heterochromatin in bovine senescent cells. *PLoS One* **6**, e26844.

Probst, A.V., Okamoto, I., Casanova, M., El Marjou, F., Le Baccon, P. & Almouzni, G. (2010) A strand-specific burst in transcription of pericentric satellites is required for chromocenter formation and early mouse development. *Dev. Cell* **19**, 625–638.

Rao, J., Bhattacharya, D., Banerjee, B., Sarin, A. & Shivashankar, G.V. (2007) Trichostatin-A induces differential changes in histone protein dynamics and expression in HeLa cells. *Biochem. Biophys. Res. Commun.* **363**, 263–268.

Shav-Tal, Y., Blechman, J., Darzacq, X., Montagna, C., Dye, B.T, Patton, J.G., Singer, R.H. & Zipori, D. (2005) Dynamic sorting of nuclear components into distinct nucleolar caps during transcriptional Inhibition. *Mol. Biol. Cell* **16**, 2395–2413.

Scheurer, M.E., Guillaud, M., Tortolero-Luna, G., McAulay, C., Follen, M. & Adler-Storthz, K. (2007) Human papillomavirus-related cellular changes measured by cytometric analysis of DNA ploidy and chromatin texture. *Cytometr. B Clin. Cytom.* **72**, 324–331.

Talwar, S., Kumar, A., Rao, M., Menon, G.I. & Shivashankar, G.V. (2013) Correlated spatio-temporal fluctuations in chromatin compaction states characterize stem cells. *Biophys. J.* **104**, 553–564.

Thomson, S., Hollis, A., Hazzalin, C.A. & Mahadevan, L.C. (2004) Distinct stimulus-specific histone modifications at hsp70 chromatin targeted by the transcription factor heat shock factor-1. *Mol. Cell* **15**, 585–594.

Unser, M. (2014) Wavelets: on the virtues and applications of the mathematical microscope. *J. Microsc.* **255**, 123–127.

Van de Wouwer, G., Scheunders, P. & Van Dyck, D. (1999) Statistical texture characterization from discrete wavelet representations. *IEEE Trans. Image Process.* **8**, 592–598.

Van De Wouwer, G., Weyn, B., Scheunders, P., Jacob, W., Van Marck, E. & Van Dyck, D. (2000) Wavelets as chromatin texture descriptors for the automated identification of neoplastic nuclei. *J. Microsc.* **197**, 25–35.

Visvanathan, A., Ahmed, K., Even-Faitelson, L., Lleres, D., Bazett-Jones, D.P. & Lamond, A.I. (2013) Modulation of higher order chromatin conformation in mammalian cell nuclei can be mediated by polyamines and divalent cations. *PLoS One* **8**, e67689.

Wang, S., Xu, J. & Zeng, J. (2015) Inferential modeling of 3D chromatin structure. *Nucl. Acids Res.* **43**, e54.

Watson, J.A., McKenna, D.J., Maxwell, P., Diamond, J., Arthur, K., McKelvey-Martin, V.J. & Hamilton, P.W. (2010) Hyperacetylation in prostate cancer induces cell cycle aberrations, chromatin reorganization and altered gene expression profiles. *J. Cell. Mol. Med.* **14**, 1668–1682.

Weyn, B., van de Wouwer, G., van Daele, A., Scheunders, P., van Dyck, D., van Marck, E. & Jacob, W. (1998) Automated breast tumor diagnosis and grading based on wavelet chromatin texture description. *Cytometry* **33**, 32–40.

Woodcock, C.L. & Ghosh, R.P. (2010) Chromatin higher-order structure and dynamics. *Cold Spring Harb. Perspect. Biol.* **2**, a000596.